A 2D Pixelated Optical Beam Scanner Controlled by the Laser Wavelength

Wim Bogaerts , *Senior Member, IEEE*, Sarvagya Dwivedi *, Member, IEEE*, Roelof Jansen, Xavier Rottenberg, and Marcus S. Dahlem , *Senior Member, IEEE*

Abstract—We present a chip-based optical beam scanner based on a dispersive optical phased array (OPA) that illuminates the far field with a pixelated pattern. To scale up the OPA to a large number of antennas, we break it up into manageable blocks with acceptable losses. The 2D wavelength scanning within a block is handled by dispersive delay lines. Between blocks, there are no delay lines, and the OPA will only have constructive interference for a discrete set of wavelengths. This results in the far-field illumination of a pixelated pattern along both x and y directions. The sidelobes and the power in the main lobe can be controlled by the power distribution of the individual OPA antennas.

Index Terms—Phased arrays, beam steering, integrated optics.

I. INTRODUCTION

OPTICAL beamforming, and particularly solid-state optical beamforming and beamsteering, has rapidly gained a strong interest, driven by applications in free-space communication and LiDAR (light detection and ranging) for the automotive industry [1]–[3]. One approach toward solid-state optical beamsteering is an optical phased array (OPA) based on a photonic integrated circuit (PIC) [4]–[10]. Photonic integrated circuits, and in particular silicon photonics, make it possible to densely integrate thousands of optical elements on the surface of a chip. In addition, they can be manufactured with great reliability in high volumes, because the technology is compatible with the infrastructure of CMOS foundries [11], [12].

While on a PIC, light is routed on the surface of the chip; on-chip optical antennas, in the form of grating couplers [13], [14], can be used to radiate the light off-chip. By arranging these antennas in 1D or 2D patterns and by controlling the amplitude and phase emitted by each antenna, an optical phased array is created. There are different optical circuit concepts to achieve beamsteering with a PIC. When a set of grating couplers is arranged in a line along the x direction, the beam of light can be steered along the corresponding θ_x direction [5], [15], [16]. The phase control between the antennas requires active phase shifters, and when the number of antennas grows into the hundreds or thousands, it becomes difficult to manage the number of individual control elements [10]. The grating coupler antennas can also be organized in a 2D periodic array along x and y, and by controlling the relative phase delay and amplitude between rows and columns, a narrow beam can be directed along the two off-chip axes [17]. Here, the 2D arrangement introduces an additional challenge of routing all the waveguides to the dense array of grating couplers and controlling the phases along both axes.

An alternative approach to 2D beam steering is to use the wavelength of light as a means to control the emission angle. Grating couplers are a diffractive structure, and the off-chip emission angle changes as a function of wavelength [13]. This can be used to scan a beam of light along one direction θ_y, as shown in Fig. 1(a). Then by organizing these grating couplers in a 1D array, the beam can be steered along the other direction θ_x using electro-optic phase shifters on each one of the waveguides feeding the grating coupler antennas [5], [8], [15], [18].

Instead of actively inducing a phase difference between every two antennas, we can feed them with differential delay lines, as shown in Fig. 1(b) [6]. Now the phase delay between the antennas will change rapidly with a wavelength sweep, which will scan the off-chip beam along the θ_x direction. In the meantime, the wavelength sweep will slowly scan the beam along θ_y because of the wavelength dependence of the grating coupler. This way, a 2D scanning pattern can be controlled with a single variable, i.e. the wavelength of the input laser. For the remainder of the paper, we will call this type of circuit a dispersive optical phased array (DOPA).

The challenge of 2D beam scanning with a DOPA is scaling it to large antenna arrays, which are needed to project a narrow beam over a long distance, e.g. for LiDAR. As we add more antennas (hundreds or thousands), the differential delays start adding up and the waveguides feeding the antennas become progressively longer. This consumes a large chip area, and induces a lot of optical propagation losses. On top of that, long waveguides will become more susceptible to errors in the phase delays, which will translate into a distortion of the emitted beam. Adding active compensation to these delay lines just translates the phase-error problem into a problem of control and power consumption.
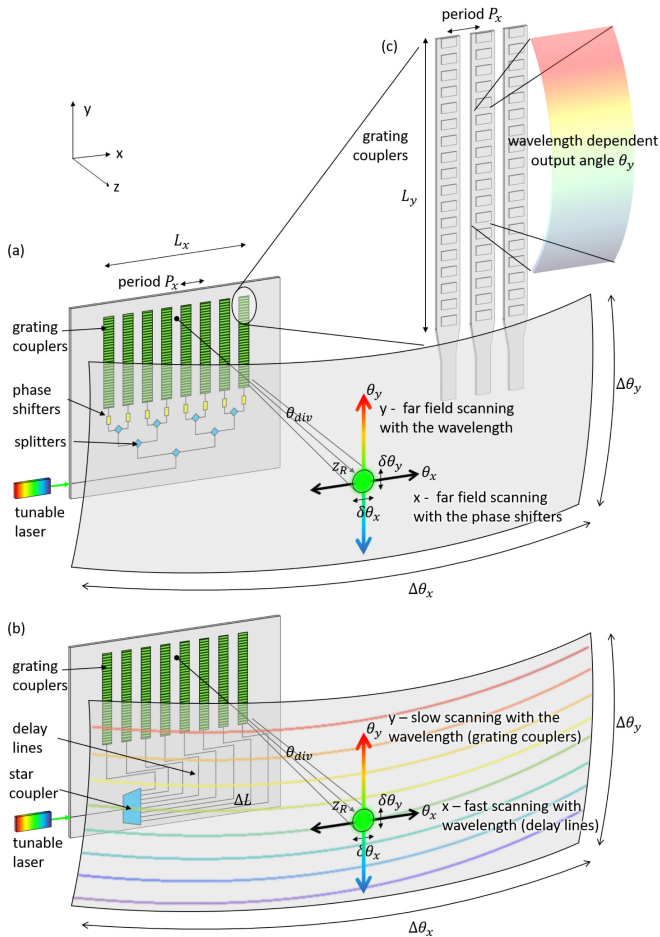
Fig. 1. Basic principle of wavelength steering with an OPA. (a) 1D scanning using active phase shifters and a grating coupler (c) with wavelength dependent output angle [5]. (b) 2D dispersive beam scanning controlled by the wavelength of the input light, as described in [6]. The scanning along the slow y-axis is governed by the dispersion of the antenna (grating coupler), while the scanning along the fast x-axis is governed by the delay length ΔL.

In this paper we propose a possible solution to this scaling problem, specifically focused at applications in LiDAR. In order to scale up a DOPA to the thousands of antennas, we subdivide the DOPA into blocks of antennas of a size where the cumulative delay lines are still manageable [19]. Each block is a smaller DOPA steering light in two directions using wavelength, and the complete circuit becomes an OPA of block antennas, fed with short, equal waveguides and thus equal phase delays. We discuss this concept based on photonic circuit simulations and calculated far-field profiles, taking into account optimistic (but still realistic) performance parameters for silicon photonics technology to evaluate the scaling potential. First, as a baseline, we look into the classical dispersive OPA, and then we extend the concept to the block-based, pixellated OPA.

II. 2D DISPERSIVE OPTICAL PHASED ARRAY SCANNER

A. Slow Scanning Along θ_y

The basic principle behind a DOPA is that we use wavelength dispersion to scan the beam along both the θ_x direction and the

θ_y direction at the same time. With a typical grating coupler antenna in silicon photonics, we can scan the beam along θ_y at a rate of $0.12°/\text{nm}$ wavelength change, and this for wavelengths around wavelengths of 1550 nm. This means we have a vertical field of view $\Delta\theta_y = 12°$ for a wavelength scanning range of $\Delta\lambda = 100$ nm (1500–1600 nm). For a typical long-range forward-looking automotive LiDAR, a vertical field-of-view (FOV) of about $20°$ is needed [2], [3], which means we would need to use two phased arrays, or a wider wavelength range, to cover the full FOV.

The length of the grating along y is dictated by the range over which we wish to project the beam. If we assume a Gaussian beam profile with waist diameter $2w_0$, the Rayleigh range z_R (i.e. length over which the beam diffracts with a factor of $\sqrt{2}$) is

$$z_R = \frac{\pi w_0^2}{\lambda} \tag{1}$$

If we assume that we need a Rayleigh range $z_R = 200$ m (this is a typical specification for long-range LiDAR in automotive [3]), and we want a well defined Gaussian beam, this implies that $L_y \approx 3 \cdot w_0 \approx 30$ mm for wavelength around 1550 nm. In the far field, the beam emitted from this antenna will diverge along θ_y with an angle θ_{div}:

$$\theta_{div} \approx 2\frac{w_0}{z_R}(\text{in radians}), \tag{2}$$

which, for our antenna, corresponds to $\theta_{div} = 0.006°$, which is much narrower than the required vertical resolution of $\delta\theta_y = 0.1°$. As a result, we are sampling the far field FOV along θ_y with approximately $\Delta\theta_y/\delta\theta_y \approx 2{,}000$ pixels, which is significantly more than the required number of scan line N_y.

To obtain such a long grating with a narrow beam, the grating profile should be weak and apodized to emit a clean (Gaussian) beam profile. This means careful engineering of a very weak grating, which is not trivial in high-contrast material systems such as silicon photonics [20], [21]. As this paper does not focus on the engineering challenge of the grating coupler itself, we will assume for the remainder of the discussion that we have such a grating coupler which we can integrate in a periodic array along the x direction.

B. Fast Scanning Along θ_x

To steer along the θ_x direction, we arrange these grating coupler antennas in a 1-D array along the x axis. We then feed these antennas with waveguide delay lines, with a constant differential delay length ΔL between every two adjacent gratings. This concept is illustrated in Fig. 1(b) [6], where we use a star coupler to distribute the optical power over the array of delay lines. Now the phase delay $\Delta\phi$ between the antennas will become dependent on the wavelength λ:

$$\Delta\phi = 2\pi\frac{\Delta L \cdot n_{\text{eff}}(\lambda)}{\lambda} \tag{3}$$

with n_{eff} the (wavelength dependent) effective refractive index of the delay line. If the delay line is long, a wavelength sweep will cause the phase delay $\Delta\phi$ to rapidly cycle through the $[0, 2\pi]$ interval, which will scan the beam along the θ_x direction. The
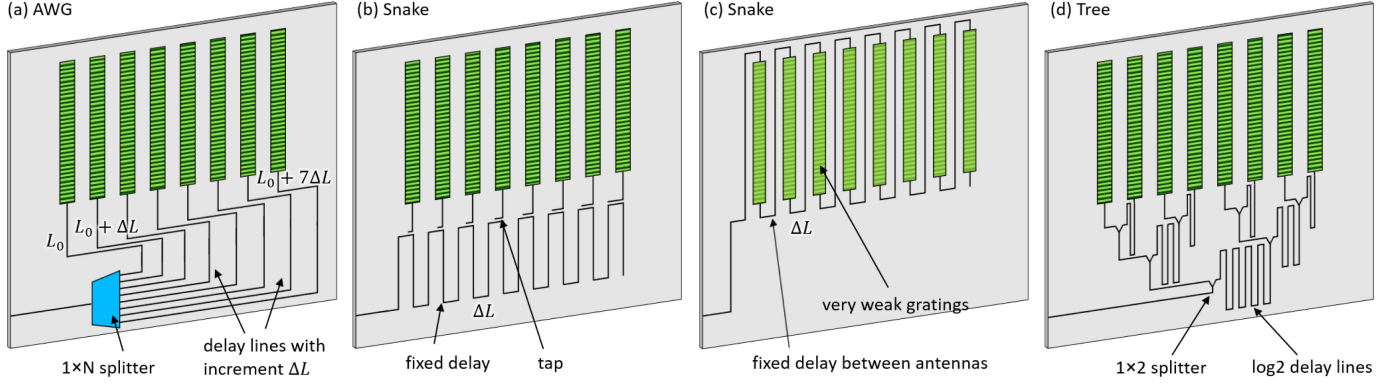
Fig. 2. Different circuit architectures to implement the incremental delays of a DOPA. (a) Arrayed waveguide grating (AWG) where the light is split over N_x waveguides with increasingly long length [6]. (b) Snake, where light is tapped off at fixed distances ΔL. (c) An alternative implementation of Snake [22], [23], where the grating is part of the delay and taps off the light directly. (d) Imbalanced splitter tree, where in each stage m a delay $2^m \cdot \Delta L$ is added in one arm.

free spectral range (FSR) for the θ_x scan can be approximated by:

$$FSR_x \approx \frac{\lambda^2}{n_g \cdot \Delta L}, \qquad (4)$$

with n_g the group index of the delay lines, which captures the first-order dispersion of n_{eff}. In the vertical direction, the angular distance $\delta\theta_y$ between two horizontal scan lines is

$$\delta\theta_y = \frac{FSR_x}{\Delta\lambda}\Delta\theta_y, \qquad (5)$$

which means we can fit in $N_y = \Delta\lambda/FSR_x$ scan lines in the vertical field of view $\Delta\theta_y$. As a result, we get a discrete sampling of the far field along θ_y. If we want a scan with higher vertical angular resolution, we need to reduce FSR_x, which implies that we need to increase ΔL, i.e. use longer delay lines between the grating couplers.

Along θ_x, the scanning of a DOPA is continuous. The scanning range (or field of view) along θ_x depends on the periodic spacing P_x of the grating couplers. We define the FOV $\Delta\theta_x$ as the angular span where the antenna array with period P_x has only a single radiation lobe:

$$\Delta\theta_x = 2a\sin\frac{\lambda}{2 \cdot P_x} \qquad (6)$$

Generally, for a forward-looking automotive LiDAR, a horizontal field of view of $25 - 50°$ is needed. For the discussion in this paper, we assume $\Delta\theta_x = 25°$. This translates in an antenna spacing $P_x = 3.47\mu m$. We chose this number because this period is manufacturable with waveguide-based antennas, and two such phased arrays side-by-side can then cover the typical horizontal field of view of $50°$ required for forward-looking long-range LiDAR [3].

If we want a similar divergence θ_{div} of the beam along the θ_x as along the θ_y direction, the array needs to have a similar size of $L_x = L_y = 30$ mm. This implies that the number of antennas N_x becomes very large:

$$N_x = \frac{L_x}{P_x} \approx 8,700 \qquad (7)$$

In the further examples, we will round this number down to 8,192 (2^{13}). The resulting beam, with a divergence $\theta_{div} = 0.006°$ will sample the horizontal field of view $\Delta\theta_x = 25°$ with approximately 4,100 pixels.

C. Implementation of the Delay Lines

The concept of the DOPA requires that we connect the many antennas with differential delay lines. In the original concept of the DOPA [6] this was accomplished with an arrayed waveguide grating: light was split using a star coupler or a splitter tree and then routed through a bundle of waveguides with incremental length [6]. This concept, shown in Fig. 2(a), works well for a small number of antennas N_x, but rapidly grows out of proportion for a larger number: the cumulative footprint of the waveguide scales with N_x^2.

Alternatively, the delays can be implemented in a snakelike geometry (Fig. 2(b-c)), where some light is tapped off after each antenna while the waveguide continues to the next grating coupler. The taps can be implemented as (tunable) directional couplers, or the grating coupler can be embedded inside the waveguide and immediately radiate the light off-chip [19], [22], [23]. The snake-like concepts scales much better, as the total waveguide area scales linearly with N_x. The challenge in this implementation is to control the tapped power accurately. In the first antennas the tapped power must be very low to make sure enough light can propagate all the way to the last antennas, where the taps should preferably couple all the remaining power. Also, the taps should have a very low loss, because on an average the light has to propagate through $N_x/2$ taps (some light is tapped off early, while some light has to propagate all the way to the final tap.) In the case where the grating coupler is embedded in the waveguide, ideally the grating strength is similarly tuned as the taps, which is a very challenging design proposition.

A third possible implementation is the imbalanced tree architecture [19] shown in Fig. 2(d). This takes the middle ground between the AWG and the Snake architecture. Light is progressively split in two, where one half propagates through a long delay line, before both are being split again. The length of the delay lines scale with powers of two, and as a result the

TABLE I
DESIGN PARAMETERS OF THE DISPERSIVE OPA

Wavelength			
Center wavelength	λ_0	1550	nm
Wavelength span	$\Delta\lambda$	100	nm
Beam specifications			
Rayleigh range	z_R	200	m
Beam divergence (for λ_0)	θ_{div}	0.006	°
Horizontal FOV	$\Delta\theta_x$	25	°
Vertical FOV	$\Delta\theta_y$	12	°
Horizontal resolution	$\delta\theta_x$	0.1	°
Vertical resolution	$\delta\theta_y$	0.1	°
Grating specifications (θ_y)			
Length of grating	L_y	28.5	mm
Dispersion of grating	$\partial\theta_y/\partial\lambda$	0.12	°/nm
OPA specifications (θ_x)			
Period of OPA	P_x	3.47	μm
Number of periods	N_x	8,192	
Number of scan lines	N_y	120	
Free spectral range	FSR_x	0.83	nm
Waveguide properties			
Waveguide eff. index (1500 nm)	n_{eff}	2.44	
Waveguide eff. index (1600 nm)	n_{eff}	2.3	
Waveguide group index	n_g	4.54	
Waveguide loss	α_{wg}	0.2	dB/cm
Waveguide spacing	s_{wg}	2.5	μm
Delay length	ΔL	634	μm
Directional coupler loss	α_{dc}	0.03	dB

differential delay between every two neighboring antennas ends up to be the same. To obtain a good power distribution over the antennas, the splitters should be imbalanced to compensate for the extra losses in the 'long' arms. But the control of these splitter ratios is much less delicate than in the Snake circuit. Also, the coupler loss is less critical, as the light only passes through $\log_2 N_x$ couplers. The Tree architecture consumes more waveguide area though, scaling proportional to $N_x \cdot \log_2 N_x$.

These different architectures can be combines, for instance, by first using several stages of an imbalanced tree and finally a snake, or by making cascading arrayed waveguide gratings in a generalized version of an imbalanced tree [24].

D. Simulation Method

In this work, we used simulations to evaluate the performance of different configurations of optical phased arrays. This uses a combination of optical circuit simulation and spatial Fourier transformations. The optical circuits, consisting of mostly of waveguides and splitters, are simulated using the Caphe circuit simulator by Luceda photonics. The field profile of the individual antennas is assumed to be a truncated Gaussian (we do not look into the design and the optimization of this building block here), and the far-field is calculated using a Fourier transform, as shown in Fig. 3. In these simulations, we do not yet consider the effects of polarization, assuming that the light emitted from the grating antennas is linearly polarized parallel to the grating lines.

E. Example

As an example, we will use a DOPA with the parameters listed in I , assuming state-of-the-art silicon photonics technology with waveguide losses of 0.2 dB/cm. We use a square emitting aperture of 28.5×28.5 mm², with 8,192 antennas (which is a
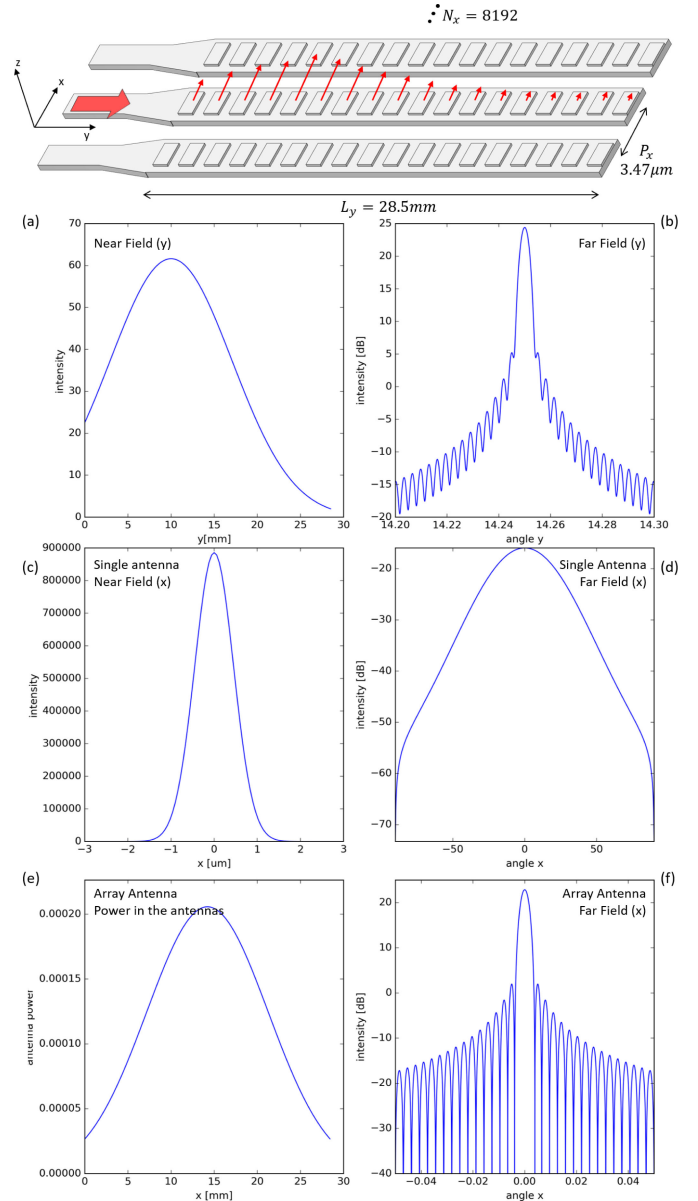

Fig. 3. Field profile of the antenna used for the simulation example. (a)–(b) Near-field/far-field above a single antenna along the y/θ_y direction. (c)–(d) Near-field/far-field above a single antenna along the x/θ_x direction. (e) Amplitudes of the individual antennas along the x direction. (f) Far-field of the array antenna along θ_x when all the elements are in phase.

TABLE II
METRICS FOR THE DIFFERENT DELAY LINES IN FIG. 2 IN A DOPA WITH 8,192 ANTENNAS, BASED ON TABLE I. WE TREAT THE TWO SNAKE-LIKE ARCHITECTURES IDENTICALLY, AS HAVE SIMILAR LOSS MECHANISMS

	AWG	Snake	Tree	
Total waveguide length	$2.1 \cdot 10^7$	5,200	33,800	mm
Insertion loss	-90	-330	-90	dB
On-chip footprint	53,200	13.0	84.4	mm²

convenient 2^{13}). The near field and far field profiles along x and y for a single antenna are shown in Fig. 3(a-d). The near field is a truncated Gaussian, which translates into a Gaussian-like far field profile with weak sidelobes. When we combine $N_x = 8,192$ antennas in an OPA, and apply a Gaussian power distribution over the antennas (Fig. 3(e)), the far field (with all
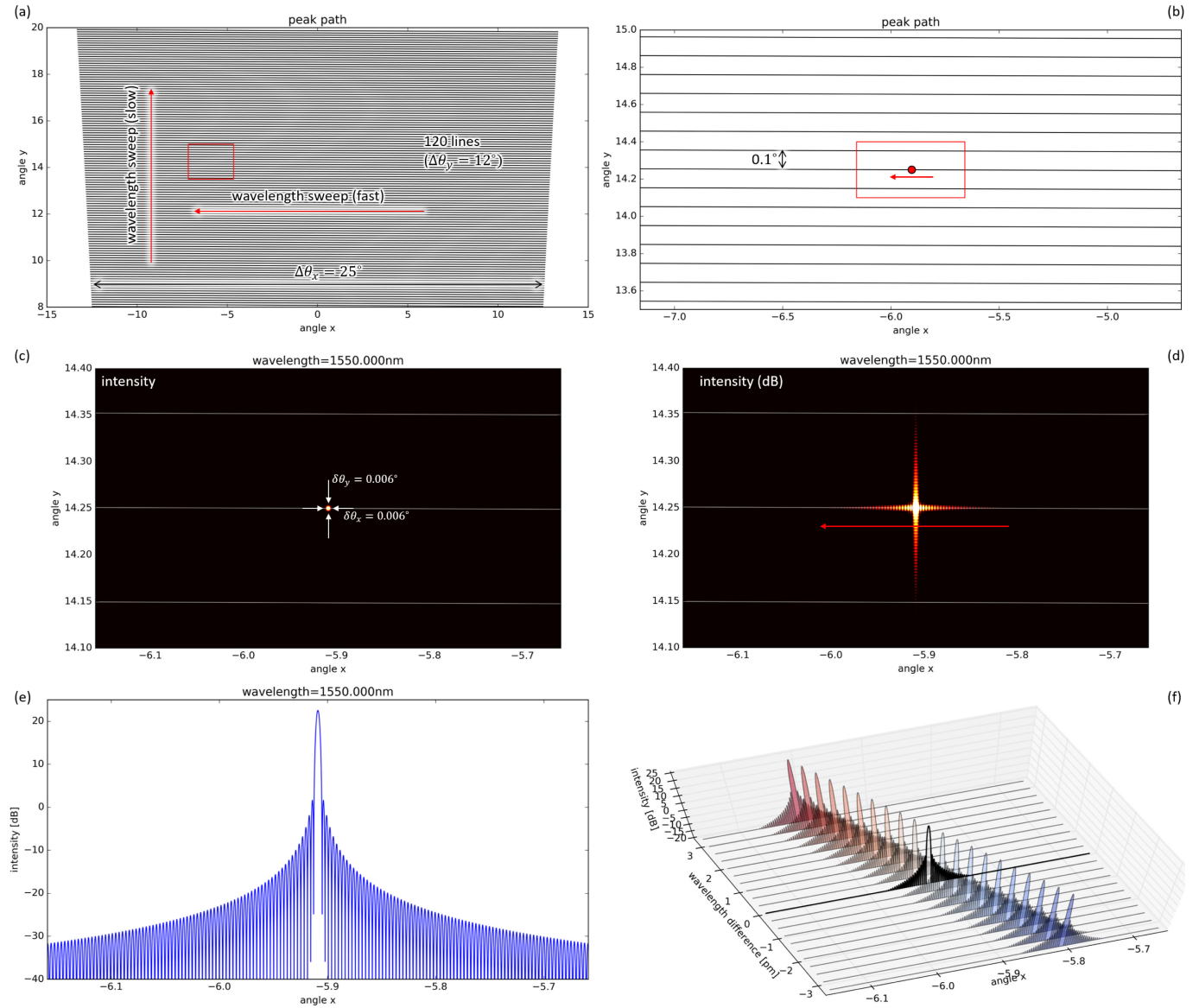
Fig. 4. Simulation of a dispersive OPA with design parameters from Table I. (a) path of the projected beam in the far field for a wavelength scan. (b) Detail of the path within the red box of (a). (c) Close-up of the farfield image at a single wavelength within the red box indicated in (b), (d) Same far-field, plotted in dB, (e) Cross section of the far field along θ_x, plotted in dB, (f) Progress of the θ_x far field profile as function of wavelength for a 6.4 pm wavelength range. We have included a supplementary video illustrating the farfield scan as function of wavelength. This is available at https://ieeexplore.ieee.org/document/9170765/media#media.

antennas in phase) is also a Gaussian with weak sidelobes, as shown in Fig. 3(f).

To apply the proper phase delay between the antennas we need to dimension the delay line. The resolution requirement of $\delta\theta_y = 0.1°$ over $\Delta\theta_y = 12°$ imposes a number of $N_y = 120$ scan lines. This gives us a free spectral range for the delay lines $FSR_x = 0.83$ nm. Using a silicon waveguide with a group index $n_g = 4.54$, according to (4) this translates into a delay between every two antennas of $\Delta L = 634\,\mu m$.

Fig. 4 shows the results of a simulation of the far field projected by this circuit. The power distribution over the antennas has a Gaussian profile, with a coverage of $6.w_0$ (in power) or $3.w_0$ (in amplitude) over the width of the antenna (with w_0 being the waist of a Gaussian beam with a Rayleigh range of $z_R = 200$ m, as specified in Eq. (1). When we increase the

wavelength (Fig. 4(c-f)), the beam scans fast from right to left, and slowly from bottom to top. The individual scan lines are not perfectly horizontal, but slowly creep along θ_y as the beam is being scanned along θ_x. We see indeed that the far field is scanned along $N_y = 120$ lines as we sweep the wavelength from 1500 nm to 1600 nm. We also see that the horizontal field of view $\Delta\theta_x$ changes with wavelength. We can expect this based on equation (6). This means that, ideally, the grating period P_x is calculated based on the shortest wavelength. A supplementary video file illustrating this positional scanning as function of wavelength is available at https://ieeexplore.ieee.org/document/9170765/media#media.

Fig. 4(c-e) shows a close-up detail of the farfield intensity, where we can clearly see that the beam divergence is smaller than $0.01°$. The profile cross section along θ_x is shown in

Fig. 4(d) on a logarithmic scale. As the power distribution over the antennas is Gaussian, we also see a Gaussian distribution in the far field. The side lobes originate from the truncation of the Gaussian. Choosing a narrower beam half-waist w_0 in the power distribution over the antennas would result in a broader divergence in the far field, but with less pronounced sidelobes. The sweep of the beam along θ_x is shown in detail in Fig. 4(f) for a wavelength sweep of only 6.4 pm around the wavelength of 1550 nm. We see that the beam scans smoothly along θ_x.

With $N_x = 8,192$ antennas, the aggregate delay length in the dispersive OPA becomes very large. This is listed in Table II. This leads to an unrealistically large footprint for the AWG, and quite substantial area consumption for the Tree architecture. Only the snake architecture has a reasonable footprint. But in the Snake the accumulated losses of the many couplers needed exacts its toll on the overall insertion loss. Clearly, even with good process technology the concept of a dispersive OPA does not scale well to large arrays.

III. PIXELATED 2D DISPERSIVE OPTICAL PHASED ARRAY SCANNER

To overcome this scaling problem, and still make it possible to implement a 2-D beam scanner controlled by the input wavelength, we separate the requirement of the range and the resolution of the farfield sampling. We do this by splitting the complete OPA in smaller blocks, each of which is a dispersive OPA with a smaller number of antennas [19]. The idea splitting up a (non-dispersive) OPA into smaller blocks is not new: in the case of an actively controlled phased array (operating at a single wavelength), using a cascade of smaller blocks can dramatically lower the number of control elements needed to drive all the antennas [10].

For the dispersive OPA, the partitioning in blocks has a somewhat different effect: partitioning the OPA in blocks breaks the phase relation between all antennas as the wavelength is swept, which will result in a pattern of discrete pixels in the far field.

A. Operating Principle

Sampling the far field with $4,100 \times 2,000$ pixels is actually more than the 250×120 pixels that are needed: the requirements in Table I list a resolution of $0.1°$, which is more than $10\times$ more coarse than the $0.006°$ that our DOPA currently samples. To realize this resolution, according to (1) we would only need a beam width of $L_x = 0.89$ mm, which corresponds to only $N_x' = 254$ antennas. This can be understood intuitively: We want to resolve ~ 250 optical modes in the far field. Our OPA is then essentially a linear mode converter that converts ~ 250 on-chip waveguide modes into ~ 250 modes in the far field. While there are of course many more modes in the far field, these will only be weakly excited.

Therefore, instead of using a DOPA with $N_x = 8,192$, we start from an DOPA with $N_x' = 256$ (2^8) antennas. Because we still need to project the beam over a range of $z_R = 200$ m, we now compose a larger optical phased array consisting of $M = 32$ of these smaller DOPAs, which together have the same

number of $N_x = 8,192$ antennas. We feed these 32 blocks with a balanced splitter tree so their inputs are in phase for all wavelengths.

Of course, this scheme breaks the sequence of incremental delays between the individual grating coupler antennas. While within a block the phase between antennas is changing as function of wavelengths, the phase between the blocks is different. The distribution can be implemented without phase control between the blocks, and it can be extracted using a calibration routine [23]. Alternatively, as we do it here, we use a balanced splitter tree to connect the input to all the blocks, keeping the inputs of the blocks at the same phase, irrespective of the wavelength. As a result, the scanning beams of the blocks only interfere constructively near the specific condition where the phase delay between antennas within a block is the same as the phase difference between the last and first antenna of adjacent blocks. This is illustrated in Fig. 5(b). If we use the phase of the first antenna of block 1 as a reference ($\phi_1 = 0$), then we find that within a block

$$\phi_{i+1} = \phi_i + \Delta\phi = \phi_i + 2\pi \frac{\Delta L n_{\text{eff}}(\lambda)}{\lambda} \quad (8)$$

The last element of a block with N_x' elements therefore has a phase $\phi_{N_x'}$:

$$\phi_{N_x'} = (N_x' - 1)\Delta\phi = 2\pi(N_x' - 1)\frac{\Delta L.n_{\text{eff}}(\lambda)}{\lambda} \quad (9)$$

Because all the blocks are injected with equal phase, the next antenna in the array will have $\phi_{N'+1} = \phi_1 = 0$. To have all the N_x antennas in phase, the phase difference between $\phi_{N'+1}$ and $\phi_{N'}$ should be equal to the $\Delta\phi$ within a block, give or take an integer number m of 2π.

$$\phi_{N_x'+1} - \phi_{N_x'} = \Delta\phi \pm m.2\pi \quad (10)$$

$$0 - (N_x' - 1)\Delta\phi = \Delta\phi \pm m.2\pi \quad (11)$$

$$N_x'\Delta\phi = \pm m.2\pi \quad (12)$$

This can be rewritten as

$$N_x'\frac{\Delta L \cdot n_{\text{eff}}(\lambda)}{\lambda} = m, \quad (13)$$

This means that we will only get constructive interference for discrete wavelengths where

$$\lambda = \frac{N_x'}{m}\Delta L \cdot n_{\text{eff}}(\lambda). \quad (14)$$

Given that $\Delta L \gg \lambda$ this is only valid for very large values of m. If we calculate the value of m for the shortest and longest wavelength used in our scanning system, then we find

$$m_{1500} = \frac{256}{1.5\mu m} \cdot 634\mu m \cdot 2.44 = 264,014 \quad (15)$$

$$m_{1600} = \frac{256}{1.6\mu m} \cdot 634\mu m \cdot 2.3 = 233,312 \quad (16)$$

which gives us 30,703 valid solutions within our wavelength sweep. This matches closely the $250 \times 120 = 30,000$ points in the far field which we want to resolve.
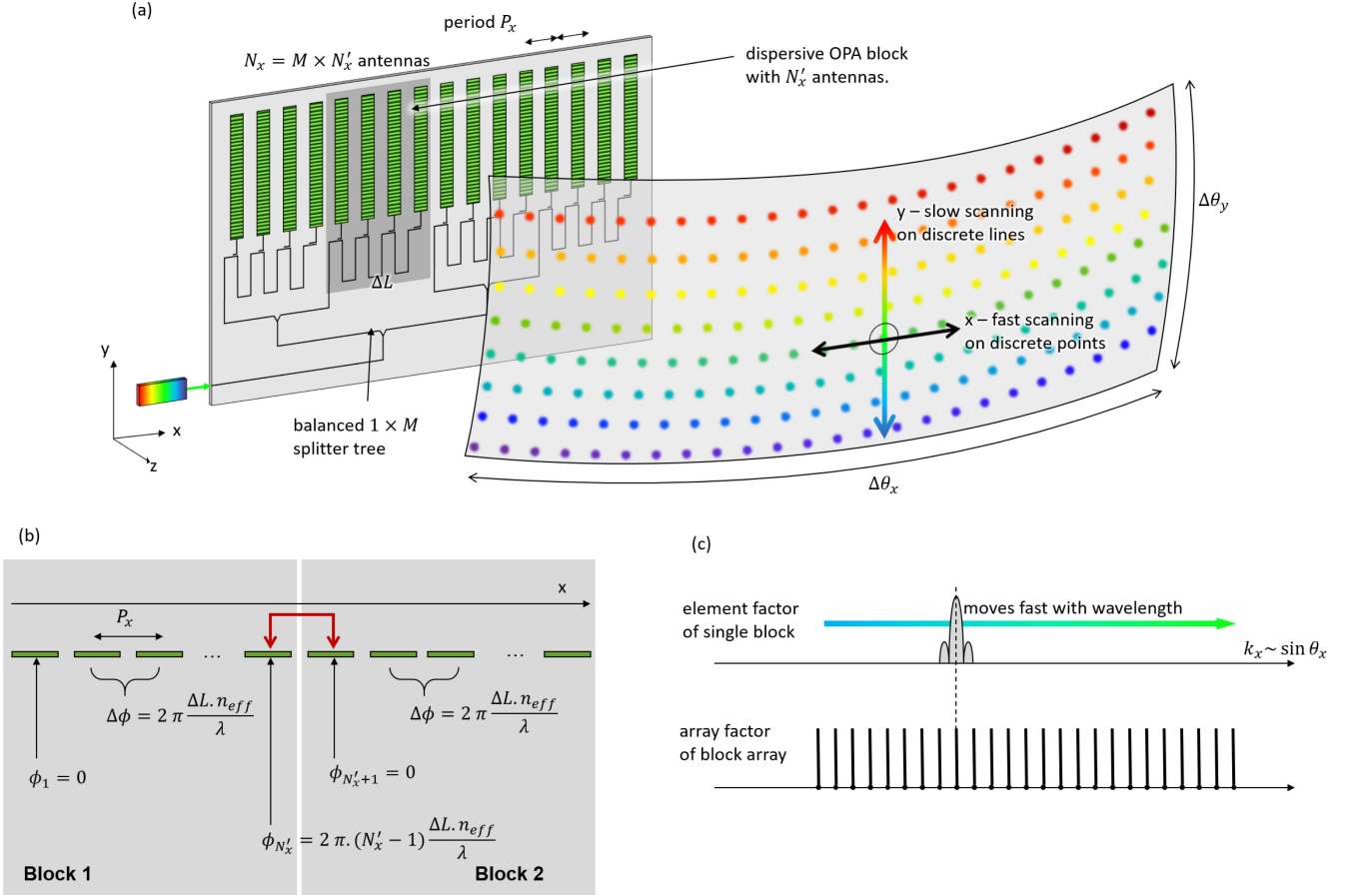
Fig. 5. Discretized dispersive optical phased array. (a) Schematic structure, where each block consists of a snake-like OPA. It is also possible to use a Tree or AWG-like OPA in each block. (b) Condition when all antennas are in phase, and (c) overlap of scanning beam of single block with diffraction orders of the large array.

We can look at this from another perspective. The complete system is essentially a periodic OPA consisting of 32 large block antennas. Because these blocks are spaced $N'_x \cdot P_x = 0.89$ mm apart, this OPA has a lot of valid diffraction orders. The element in this array is itself a dispersive OPA, so its element function will scan along θ_x as function of wavelength. Every time this scanning beam aligns with a valid diffraction order of the larger OPA, a narrow beam will be formed. This essentially illuminates a discrete grid of pixels in the far field. Therefore, we call this type of dispersive OPA a 'pixelated dispersive OPA'.

B. Example

Let's build on the previous example, and construct a pixelated dispersive OPA with $M = 32$ blocks of $N'_x = 256$ antennas each. The blocks are arranged such that the antennas form a uniform array, i.e. the spacing between the blocks is the same as the spacing between the antennas. The power over the antennas has the same Gaussian distribution as in Fig. 3(e).

Fig. 6 shows the simulation results of the far field for this circuit (a supplementary video file is available at https://ieeexplore.ieee.org/document/9170765/media#media). The peak of the beam no longer moves continuously along θ_x when we sweep the wavelength. Instead, we see peaks at discrete angles θ_x,

TABLE III
DESIGN PARAMETERS OF THE PIXELATED DISPERSIVE OPA

Single block			
Period of OPA	P_x	3.47	μm
Number of antennas	N'_x	256	
Total array			
Number of blocks	M	32	
Number of antennas	N_x	8,192	

TABLE IV
METRICS FOR THE DELAY LINES IN FIG. 2, BUT NOW FOR A 32×256
PIXELATED DOPA BASED ON TABLE I AND III

	AWG	Snake	Tree	
Waveguide length per block	20,700	162	650	mm
Footprint per block	51.8	0.4	1.62	mm^2
Total waveguide length	663,000	5,200	20,800	mm
Insertion loss	-2.11	-6.7	-2.11	dB
On-chip footprint	1,660	13.0	52.0	mm^2

and for the wavelengths where all antennas are in phase, these peaks become identical to the peaks of the full OPA shown in Fig. 4. Between these wavelengths, we see that the power becomes mostly distributed over the peaks, with some power in the sidelobes between the peaks.
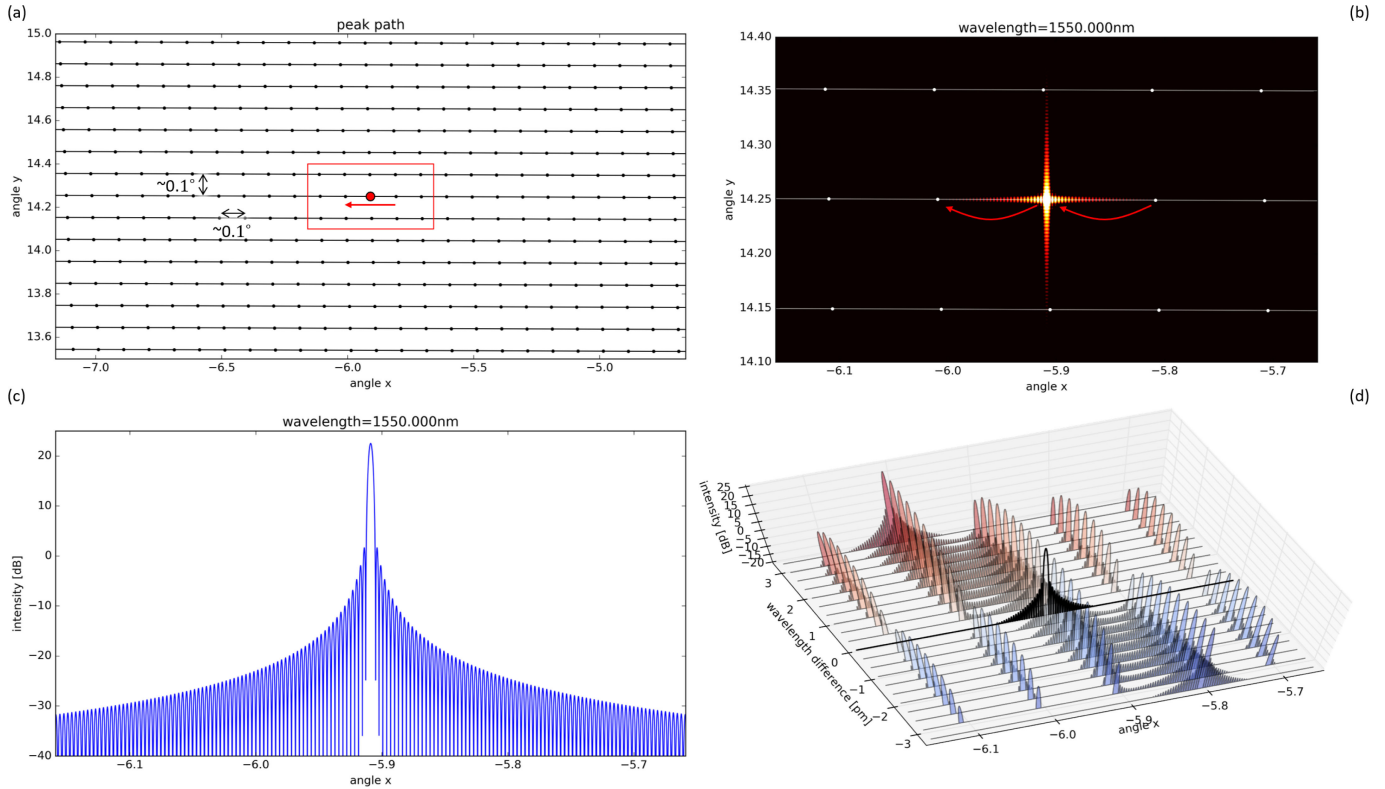
Fig. 6. Simulated farfield of the pixelated dispersive OPA, with similar antenna amplitudes (Gaussian distribution) as the dispersive OPA from Fig. 4. (a) Trajectory of the peak in the far field, with the conditions for constructive interference. (b) Farfield intensity (in dB) at the peak indicated with the red dot in (a). (c) Cross section along θ_y of the field in (b). (d) Evolution of the θ_x far field as function of wavelength along the red arrow in (a)–(b). We have included a supplementary MP4 video illustrating the farfield scan as function of wavelength. This is available at https://ieeexplore.ieee.org/document/9170765/media#media.

Table IV shows the resulting performance metrics for the delay lines when we use an AWG, Snake or Tree, using the waveguide properties from Table I. Thanks to the subdivision into blocks, the footprint and insertion losses have been lowered to realistic proportions, as the amount of delay lines and power splitters has been reduced dramatically.

C. Power Distribution Over the Array

In the previous example, we used a Gaussian power distribution over the antennas. This gives us a well defined Gaussian beam (with small sidelobes) when all the antennas are in phase. But it is not straightforward to distribute the light over the antennas in such a distribution: first the power must be distributed unevenly over the blocks, and then the distribution within a block is different for each block.

Some alternative power distributions are shown in Fig. 7. Except for the top profile, which corresponds to the previous example and the plots in Fig. 6, all the other cases have the same power distribution within a block. This makes it possible to design all the blocks to be identical, reducing the complexity in balancing all the couplers and the optical path lengths.

We see that of these cases, the distribution in Fig. 7(d), which approximates most the Gaussian from Fig. 7(a) and Fig. 6, has the lowest sidelobes. In this distribution, the power inside the blocks is distributed uniformly over all antennas, while the

splitter tree that distributes the power over the blocks requires a Gaussian distribution.

The more uniform distributions, which in the far field result in a sinc-like pattern, have much stronger sidelobes.

D. Power in the Main Lobe

As the wavelength is swept, the location of the peaks remains at the fixed positions, but the intensity increases and then decreases, until the power is transferred to the next peak. This means that, unlike in the continuous dispersive OPA, the power in the main lobe is not constant, but it will oscillate with wavelength, as shown in Fig. 8.

We see that the most Gaussian distribution profiles attain the same peak power as the continuous dispersive OPA for the wavelengths where all antennas are in phase. For other wavelengths, the power in the main lobe drops until it is picked up by the next farfield pixel.

IV. DISCUSSION

The pixelated dispersive OPA offers a way to scale up a passive dispersive OPA to a large number of antennas without incurring excessive losses. While we have not yet experimentally demonstrated the concept, we can already identify certain challenges and opportunities for improvements.
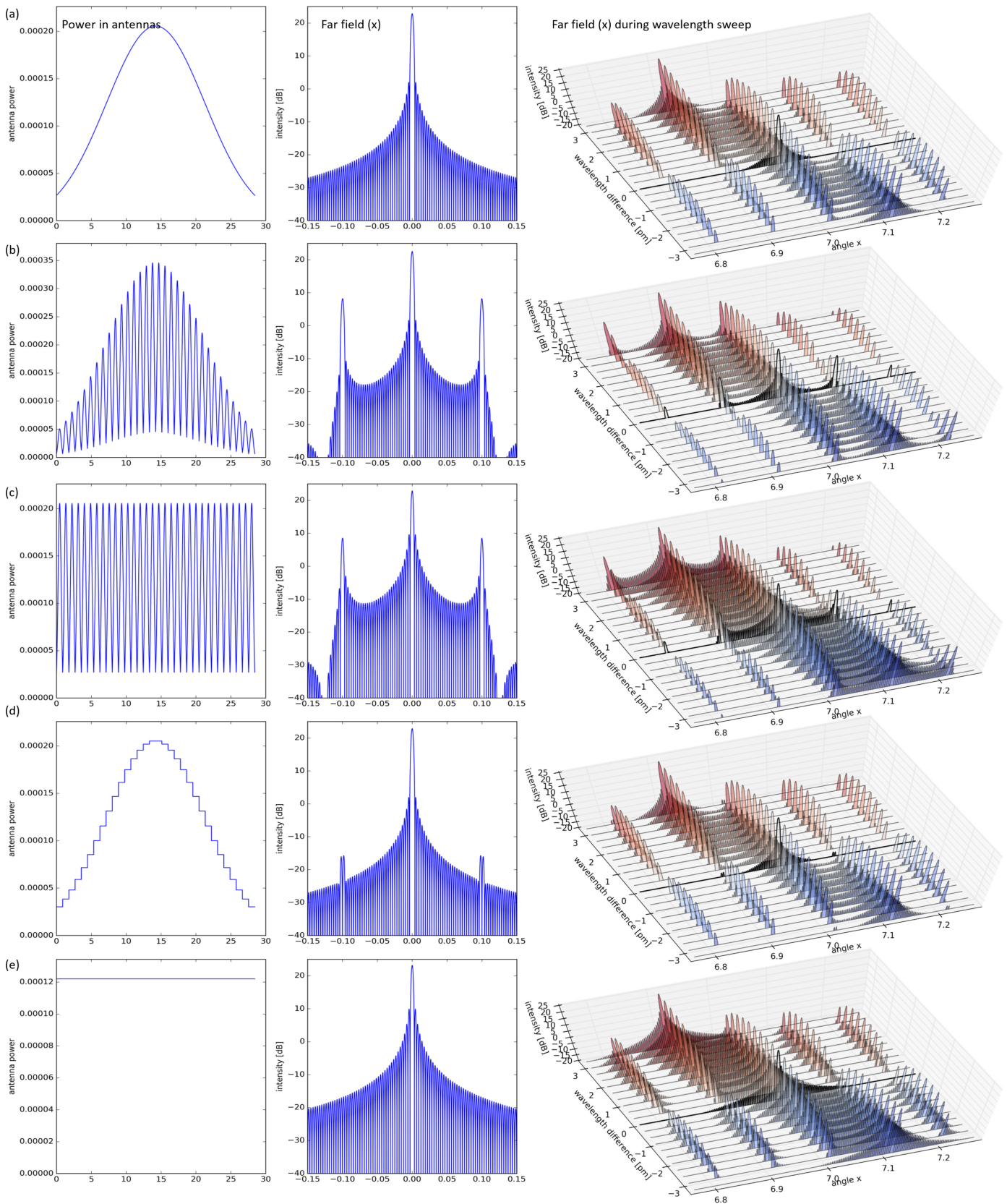
Fig. 7. Different power distribution profiles for the pixelated dispersive OPA, the resulting far field profile when all the antennas are in phase, and the evolution of the far-field when sweeping the wavelength. (a) Gaussian profile over all antennas, as used in Fig. 6. (b)–(e) Different combinations of Gaussian and Uniform distributions within a block and between blocks. All power distributions are normalized for unity power.
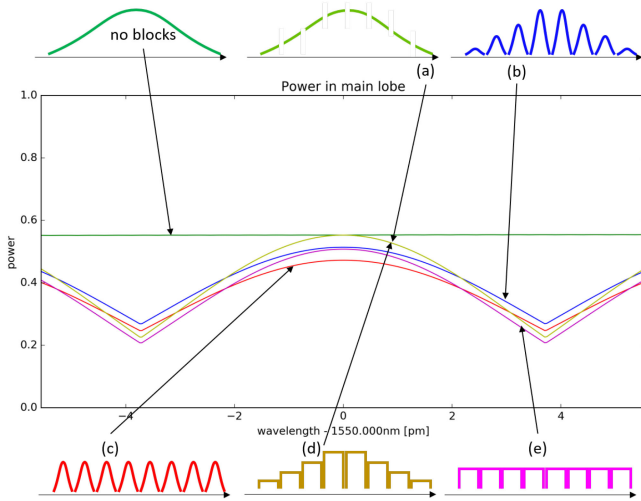
Fig. 8. Power in the main lobe for the different implementations of the dispersive OPA, depicted in Fig. 4, 6 and 7.

A. Phase Errors

The beam quality of an optical phased array depends strongly on accurate control of the relative phases of all the antennas. In the dispersive 2-D OPA (pixelated or not) the phase is entirely controlled by the optical path length in the delay lines. These delays are quite long, and we can expect that phase errors can accumulate along the lines. These can be due to fabrication variations and line-width roughness, increasing in a random-walk fashion proportional to $\sqrt{L}$, as described in [25]. In high-contrast material systems such as silicon, these phase errors have proven detrimental in much smaller arrayed waveguide gratings [26], so extremely good fabrication technology is needed, or a lower-contrast waveguide system such as silicon nitride [27], [28]. Other, more systematic phase errors can be induced by long-range fabrication variations over the wafer [29] or temperature gradients over the chip. From first estimates, a temperature difference between two silicon delay lines $5°C$ can induce a π phase shift at the output antennas. This means that either the temperature uniformity needs to maintained with $\ll 1°C$ precision, or the delay lines should be designed with lower temperature sensitivity [30].

Still, this means that, even though the OPA circuit is passive, it will probably require some active tuning to keep all the antennas in phase. This tuning can be slow and is only needed to compensate static or slowly-varying phase errors. Low-power techniques such as liquid-crystal [31], piezo-electric effects [32] or MEMS [33], [34] could be suitable.

B. Gaps Between the Pixels

Because the OPA is partitioned in blocks, the farfield is only illuminated in discrete directions, and the main beams remain focused on these locations. Therefore, the spaces between these locations are not illuminated, or only catch light from the side-lobes, which are orders of magnitude below the power of the main peak.

The ratio between the illuminated areas and the blind zones along the θ_x direction depends on the number of blocks M. More and smaller blocks will result in fewer valid diffraction orders, and therefore pixels that are spaced further apart.

If we translate this to the specifications of the LiDAR in Table I, with a Rayleigh range $z_R = 200$ m, then we find that the illuminated spot is approximately 40 mm in diameter, while the pixels are spaced 35 cm apart. For automotive applications, this means that objects narrower than 35 cm could be missed.

C. Filling the Gaps With Active Tuning

It is possible to illuminate the blind areas by shifting the pixelated pattern. This can be done by manipulating the phase $\Delta\phi_{block}$ in eq. (10). When we add an active phase shifter in front of every block, and apply a constant phase difference between every two blocks, the grid of valid diffraction orders will shift. This can be used to shift the peaks back and forth, addressing the far-field locations in between the pixels along the θ_x direction. Along the θ_y direction, the beam can be shifted by modulating the refractive index of the grating coupler antennas, e.g. by heating them.

D. Using More (Smaller) Blocks

We have discussed how we reduce the prohibitively high losses of a large phased array by partitioning it into smaller blocks. Here, we chose 32 blocks because that gives us the correct amount of horizontal pixels in the far field. Using a larger number of smaller blocks would push down the losses even further, but at the cost of fewer horizontal pixels.

Using the active tuning could help to overcome this limitation, as it would become possible to shift the pixel pattern horizontally to scan the gaps between the pixels, effectively boosting the horizontal resolution. The trade-offs between the benefits and drawbacks of this technique merit further study.

E. Wavelength-Dependent Field of View

As can be seen from Fig. 4(a), the horizontal field of view of the DOPA changes with θ_y. This is easy to understand, as the horizontal field of view is determined by the ratio of the antenna period P_x and the wavelength. As the angle θ_y is related to the wavelength, the field of view will increase for longer wavelengths and therefore larger angles. This is not a fundamental problem, but when designing the OPA, it is important to design the field of view for the shortest wavelength.

The wavelength dependence also applies for the spacing between the pixels along the θ_x direction. For longer wavelengths, the pixel spacing will increase. Also, the far-field pixel spacing is not uniform along θ_x. Because the pixels correspond to diffraction orders, they are spaced uniformly along $sin\theta_x$. This means that for wider angles, the pixels will be spaced further apart.

F. Wavelength Scanning and FMCW LiDAR

One particular implementation of LiDAR uses the frequency modulated continuous wave (FMCW) technique. This uses a

frequency modulation on the emitting laser beam, which makes it possible to deduce the roundtrip time of the light from the frequency difference between the return light and the local oscillator [1].

The proposed scheme is compatible with the use of FMCW. For scanning the farfield a wavelength sweep is applied. By choosing the sweep rate correctly, this wavelength scanning can be used directly as the linear frequency ramp used in FMCW. Alternatively, a custom additional frequency modulation can be imposed onto the scanning laser wavelength. The FMCW needs sufficient bandwidth or dwell time per pixel to resolve the range with sufficient accuracy. In the continuous dispersive OPA implementation, this can be a problem, as the wavelength scanning induces a continuous movement of the main emission lobe, and the pixels become 'smeared out'. In the pixelated approach discussed here, the main lobe is targeted at discrete positions where it dwells until an adjacent pixel is being illuminated. This provides a larger dwell time on the same location.

V. CONCLUSION

We presented a concept for an optical phased array which illuminates the far field in a pixelated way by scanning the wavelength. Using an OPA with dispersive delay lines between the antennas, a sweep of the wavelength will scan a beam in the far field fast along the θ_x direction. In combination with a grating coupler with a wavelength dependent θ_y emission angle, a 2-D line scan is possible. Because this concept does not scale well for large arrays, even with alternative configurations of delay lines, we extended this concept by partitioning the dispersive OPA in smaller blocks, each a dispersive OPA. Thse blocks then form a larger OPA which illuminates discrete pixels in the far field.

The density and size of the pixels can be configured through the pitch P_x of the array antennas, the number of blocks M and the number of antennas per block N'_x. The pixelated OPA allows us to decouple the requirements for Rayleigh range and for scanning resolution.

We demonstrated this concept with an example of 8,192 antennas, by partitioning the array into 32 blocks of 256 antennas. The result is a farfield image of 250×120 pixels over a $25° \times 12°$ field of view.

APPENDIX

REFERENCES

[1] B. Behroozpour, P. A. Sandborn, M. C. Wu, and B. E. Boser, "Lidar system architectures and circuits," *IEEE Commun. Mag.*, vol. 55, no. 10, pp. 135–142, Oct. 2017.

[2] C. Pulikkaseril and S. Lam, "Laser eyes for driverless cars: the road to automotive LIDAR," in *Proc. Opt. Fiber Commun. Conf.*, 2019, Paper Tu3D.2.

[3] J. Hecht, "Lidar for self-driving cars," *Opt. Photon. News*, vol. 29, no. 1, pp. 26–33, 2018.

[4] M. J. Heck, "Highly integrated optical phased arrays: Photonic integrated circuits for optical beam shaping and beam steering," *Nanophotonics*, vol. 6, no. 1, pp. 93–107, 2017.

[5] K. Van Acoleyen *et al.*, "Off-chip beam steering with a one-dimensional optical phased array on silicon-on-insulator," *Opt. Lett.*, vol. 34, no. 9, 2009, Art. no. 1477.

[6] K. V. Acoleyen, W. Bogaerts, and R. Baets, "Two-dimensional dispersive off-chip beam scanner," *IEEE Photon Technol. Lett.*, vol. 23, no. 17, pp. 1270–1272, Sep. 2011.

[7] M. R. Watts, "Towards an Integrated Photonic LIDAR Chip," in *Proc. Imag. Appl. Opt.*, 2015, Paper AIW4C.1.

[8] S. A. Miller *et al.*, "512-Element actively steered silicon phased array for low-power LIDAR," in *Proc. Conf. Lasers Electro-Opt.*, 2018, vol. 1, pp. 1–2.

[9] C. V. Poulton *et al.*, "Long-range LiDAR and free-space data communication with high-performance optical phased arrays," *IEEE J. Sel. Topics Quantum Electron.*, vol. 25, no. 5, Sep./Oct. 2019, Art. no. 7700108.

[10] S. Chung, H. Abediasl, and H. Hashemi, "A monolithically integrated large-scale optical phased array in silicon-on-insulator CMOS," *IEEE J. Solid-State Circuits*, vol. 53, no. 1, pp. 275–296, Jan. 2018.

[11] X. Chen *et al.*, "The emergence of silicon photonics as a flexible technology platform," *Proc. IEEE*, vol. 106, no. 12, pp. 2101–2116, Dec. 2018.

[12] A. Rahim, T. Spuesens, R. Baets, and W. Bogaerts, "Open-access silicon photonics: Current status and emerging initiatives," *Proc. IEEE*, vol. 106, no. 12, pp. 2313–2330, Dec. 2018.

[13] D. Taillaert *et al.*, "An out-of-plane grating coupler for efficient butt-coupling between compact planar waveguides and single-mode fibers," *IEEE J. Quantum Electron.*, vol. 38, no. 7, pp. 949–955, Jul. 2002.

[14] G. Roelkens, D. Vermeulen, D. Van Thourhout, and R. Baets, "High efficiency diffractive grating couplers for interfacing a single mode optical fiber with a nanophotonic silicon-on-insulator waveguide circuit," *Appl. Phys. Lett.*, vol. 92, no. 13, 2008, Art. no. 131101.

[15] J. C. Hulme *et al.*, "Fully integrated hybrid silicon two dimensional beam scanner," *Opt. Exp.*, vol. 23, no. 5, 2015, Art. no. 5861.

[16] J. K. Doylend *et al.*, "Two-dimensional free-space beam steering with an optical phased array on silicon-on-insulator," *Opt. Express*, vol. 19, no. 22, 2011, Art. no. 21595.

[17] J. Sun, E. Timurdogan, A. Yaacobi, E. S. Hosseini, and M. R. Watts, "Large-scale nanophotonic phased array," *Nature*, vol. 493, no. 7431, pp. 195–199, 2013.

[18] W. Guo *et al.*, "Two-dimensional optical beam steering with InP-based photonic integrated circuits," *IEEE J. Sel. Topics Quantum Electron.*, vol. 19, no. 4, Jul./Aug. 2013, Art. no. 6100212.

[19] W. Bogaerts, M. Dahlem, S. Dwivedi, R. Jansen, and X. Rottenberg, "Dispersive optical phased array circuit for high-resolution pixelated 2D far-field scanning controlled by a single wavelength variable," *Proc. SPIE*, 2020, vol. 11284, pp. 11 284–69.

[20] M. Verbist, W. Bogaerts, and D. Van Thourhout, "Design of weak 1-D bragg grating filters in SOI waveguides using volume holography techniques," *J. Lightw. Technol.*, vol. 32, no. 10, pp. 1915–1920, May 2014.

[21] T. Zhu, Y. Hu, P. Gatkine, S. Veilleux, J. Bland-Hawthorn, and M. Dagenais, "Arbitrary on-chip optical filter using complex waveguide Bragg gratings," *Appl. Phys. Lett.*, vol. 108, no. 10, 2016, Art no. 101104.

[22] B. Zhang *et al.*, "Serpentine optical phased array silicon photonic aperture tile with two-dimensional wavelength beam steering," in *Proc. Opt. Fiber Commun. Conf. Exhibition*, 2019, Paper M4E.5.

[23] N. Dostart *et al.*, "Serpentine optical phased arrays for scalable integrated photonic lidar beam steering," *Optica*, vol. 7, no. 6, pp. 726–733, 2020.

[24] F. Xiao, G. Li, and A. Xu, "Cascade arrangement of irregular optical phased arrays," *Opt. Commun.*, vol. 281, no. 8, pp. 1945–1949, 2008.

[25] T. Goh, S. Suzuki, and A. Sugita, "Estimation of waveguide phase error in silica-based waveguides," *J. Lightw. Technol.*, vol. 15, no. 11, pp. 2107–2113, Nov. 1997.

[26] S. Pathak, P. Dumon, D. Van Thourhout, and W. Bogaerts, "Comparison of AWGs and Echelle gratings for wavelength division multiplexing on silicon-on-insulator," *IEEE Photon. J.*, vol. 6, no. 5, Oct. 2014, Art. no. 4900109.

[27] R. Baets *et al.*, "Silicon photonics: Silicon nitride versus silicon-on-insulator," in *Proc. Opt. Fiber Commun. Conf. Exhibition*, 2016, pp. 3–5.

[28] P. Munoz *et al.*, "Foundry developments toward silicon nitride photonics from visible to the mid-infrared," *IEEE J. Sel. Topics Quantum Electron.*, vol. 25, no. 5, Sep./Oct. 2019, Art. no. 8200513.

[29] Y. Xing, J. Dong, U. Khan, and W. Bogaerts, "Hierarchical model for spatial variations of integrated photonics," in *Proc. IEEE Int. Conf. Group IV Photon.*, 2018, pp. 91–92.

[30] S. Dwivedi, H. D'Heer, and W. Bogaerts, "Maximizing fabrication and thermal tolerances of all-silicon fir wavelength filters," *IEEE Photon. Technol. Lett.*, vol. 27, no. 8, pp. 871–874, Apr. 2015.

[31] Y. Xing *et al.*, "Digitally controlled phase shifter using an SOI slot waveguide with liquid crystal infiltration," *Photon. Technol. Lett.*, vol. 27, no. 12, pp. 1269–1272, 2015.

[32] W. Jin, R. Polcawich, P. Morton, and J. Bowers, "Piezoelectrically tuned silicon nitride ring resonator," *Opt. Express*, vol. 26, no. 3, pp. 3174–3187, 2018.

[33] N. Quack *et al.*, "MEMS-enabled silicon photonic integrated devices and circuits," *IEEE J. Quantum Electron.*, vol. 56, no. 1, Feb. 2020, Art. no. 8400210.

[34] C. Errando-Herranz *et al.*, "MEMS for photonic integrated circuits," *IEEE J. Sel. Topics Quantum Electron.*, vol. 26, no. 2, Mar./Apr. 2019, Art. no. 8200916.

Roelof Jansen received the M.Sc. degree in electronic engineering with computer science from the University of Stellenbosch, in 2008. He joined imec, in 2007, where currently he is the Team Leader for the Photonic Microsystems team, part of the Wave-based Sensing and Actuation (WSA) group. The team specializes in systems based on integrated photonic platforms, such as optical beamformers, spectrometers, optical sensors, flat optics and more. He has more than 14 years of experience in the fields of Photonics, RF and MEMS, and has coauthored over 50 peer reviewed publications and several patents.

Wim Bogaerts (Senior Member, IEEE) received the Ph.D. degree in the modelling, design and fabrication of silicon nanophotonic components from Ghent University, in 2004. He is a Professor with the Photonics Research Group at Ghent University - imec. During this work, he started the first silicon photonics process on imec's 200 mm pilot line, which formed the basis of the multi-project-wafer service ePIXfab. Wim's current research focuses on the challenges for large-scale silicon photonics: Design methodologies and controllability of complex photonic circuits. In 2014, Wim cofounded Luceda Photonics, a spin-off company of Ghent University, IMEC and the University of Brussels (VUB). Luceda Photonics develops unique software solutions for silicon photonics design, using the IPKISS design framework. Since 2016 Wim is again Full-Time Professor at Ghent University, looking into novel topologies for large-scale programmable photonic circuits, supported by a consolidator grant of the European Research Council (ERC). Wim has a strong interest in telecommunications, information technology, and applied sciences. He is a Senior Member of OSA and SPIE.

Xavier Rottenberg received the M.Sc. degree in physics engineering and the DEA in theoretical physics from the Universit Libre de Bruxelles, in 1998 and 1999, respectively. He received the Ph.D. degree in electrical engineering from KU Leuven, in 2008. He worked one year at the Royal Meteorological Institute of Belgium in the field of remote sensing from Space. He has been at IMEC Leuven since 2000, where he contributes to research in the field of RF, RF-MEMS, photonics and microsystems modelling/integration. He currently leads the Wave-based Sensing and Actuation (WSA) Group, working among other topics on photonics, sensors, acoustics, and M/NEMS. He has coauthored over 120 peer reviewed publications and has been issued various patents. He was a Lecturer or Invited Speaker at DTIP (05), EuroSimE (08), ESREF (08), ESoA (10/12/14), RF-MEMS summer school (13), FETCH 2016, NERF Neurotechnology Symposium (16), OpenMinds (17), Nanoworkshop at Beijing University (18).

Sarvagya Dwivedi (Member, IEEE) received the master's degree in electrical engineering from the Indian Institute of Technology, Bombay, in 2009 and the Ph.D. in photonics engineering from Photonics Research Group, Ghent University Imec, Belgium, in 2016. He then worked as a Postdoc Research Associate with the University of California Santa Barbara, Santa Barbara, CA, USA. He has authored and coauthored more than 30 publications in the areas of all-silicon, silicon nitride and Ge-on-Si based tolerant devices and circuits for applications in datacom, telecom, and mid-infrared sensing. Prior to his Ph.D., he worked as an Applications Engineer and later as a Manager with COMSOL Multiphysics, where he was responsible for device and system-level solutions in the area of RF, MEMS, and heat transfer. Currently, he is working as a Senior Photonics Researcher with Imec, Belgium, developing optical phased arrays for beamforming, LiDAR and imaging. He is a Member of the OSAn and the IEEE Photonics Society. He is an Active Reviewer of IEEE PHOTONICS TECHNOLOGY LETTERS, IEEE JOURNAL OF LIGHTWAVE TECHNOLOGY, and IEEE JOURNAL OF SELECTED TOPICS IN QUANTUM ELECTRONICS, *OSA Optics Express*, and *Optics Letters*. He also served as a program Committee Member and Session Chair of the various IEEE and OSA conferences.

Marcus S. Dahlem (Senior Member, IEEE) received the Ph.D. degree in electrical engineering from MIT, in 2011, from the Optics and Quantum Electronics group at the Research Laboratory of Electronics. He joined imec, in 2018 as Principal Member of Technical Staff in the Wave-based Sensing and Actuation Group. His current focus is on photonic integrated circuits in Si/SiN for optical switching, optical beamforming and LiDAR applications. Prior to imec, he was an Associate Professor and the Director of the Center of Excellence on Integrated Photonics, the Khalifa University of Science and Technology (Abu Dhabi), which he joined in 2011 as an Assistant Professor. In 2008, he worked with IBM Zurich Research Laboratory, in the Exploratory Photonics group. Between 2003 and 2011, he worked as a Research Assistant with MIT, and in 2003 and 2005, he was also a Teaching Assistant. From 1999 to 2002, he served as a Laboratory Instructor in the Physics Department, the University of Porto (Portugal), and as a Researcher with the Institute for Systems and Computer Engineering (INESC) of Porto. He is a Member of OSA and SPIE, and has served as reviewer of several optics and photonics journals.